

Modeling of galfenol bending actuator considering nonlinear hysteresis and dynamic real-time control strategy

Liang Shu¹, Guichu Wu¹, Dingfang Chen² and Marcelo J Dapino³

¹The Key Laboratory of Low-Voltage Apparatus Intellectual Technology of Zhejiang, Wenzhou University, Wenzhou 325027, People's Republic of China

²Institute of Intelligent Manufacturing and Control, Wuhan University of Technology, Wuhan 430063, People's Republic of China

³Department of Mechanical and Aerospace Engineering, The Ohio State University, Columbus, OH 43210, USA

E-mail: shuliangalbert@163.com

Received 18 July 2015, revised 12 November 2015

Accepted for publication 25 November 2015

Published 23 February 2016



Abstract

On active bending structures, the actuation direction and the excitation field direction are not the same. Simple lumped parameter models are inadequate to describe the relationship between output displacement and input field. In this paper, a dynamic distributed parameter model is presented to describe the system dynamics of a galfenol bending actuator. To consider nonlinearities and hysteresis in bending, a nonlinear magnetomechanical model is developed to characterize the hysteretic magnetostriction generated by the galfenol layer. A dynamic real-time control strategy is proposed to compensate for hysteresis. A nonlinear inverse filter is constructed to linearize the hysteresis based on the proposed distributed parameter model. In order to increase the calculation efficiency, a new iteration method is proposed to calculate the filter. The iteration stepsize of the input field can be adaptively updated according to the inverting error. Simulation results show that significant enhancement of convergence efficiency can be achieved by using the proposed method compared with the existing fixed step size method. Experiments have been conducted to verify the real-time control strategy.

Keywords: magnetostrictive devices, real time systems, hysteresis, compensation

(Some figures may appear in colour only in the online journal)

1. Introduction

Magnetostrictive materials exhibit dimensional changes in response to magnetic fields and change magnetic state in response to external stress. These effects have been used to develop actuators and sensors for industrial [1, 2], aerospace [3, 4] and manufacturing applications [5]. Galfenol is a structural magnetostrictive material which is suitable for load-carrying transducers operating under combined loads [6, 7].

However, the inherent hysteresis of galfenol hinders its effective use, especially for dynamic applications. Model based control design is an effective way to address the nonlinear hysteresis problem for magnetostrictive transducers,

especially when the system is operating in highly hysteretic and nonlinear regimes. Model based control can be roughly subdivided into two categories [8], nonlinear control designs and linear control designs employing nonlinear inverse filters. Examples of the former can be found in [9–11]. Usually the control signal is obtained by analyzing the global stability of the system [10], or by optimizing a nonlinear cost function considering hysteresis [11], without constructing the inverse filter. The latter method consists of constructing an inverse filter to linearize the transducer behavior in the manner illustrated in figure 1. If the filter is sufficiently accurate, then the transducer output can be designed almost the same with the reference input. In this paper, we address the dynamic real-

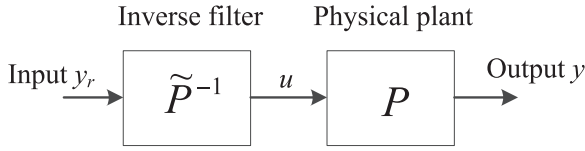


Figure 1. Concept of inverse compensation.

time control problem of a galfenol bending actuator by employing the concept of inverse compensation.

Different models have been used to implement inverse compensators. The filters are developed by using neural network identification [12] or the Prandtl–Ishlinskii hysteresis operator [13]. In [14–17], the inverse compensators are implemented with Preisach operators. The nonmonotonic hysteresis problem is solved in [14] by using inverse compensation. The nonmonotonic hysteresis is modeled by combining a monotonic Preisach hysteresis operator and a quadratic operator. In [17], the persistent excitation conditions for parameter convergence are discussed and the recursive identification technique is developed to construct the compensator. Another fixed point and closest-match algorithm is presented in [16] to approximately invert the operator. These methods are suitable for applications when only hysteresis is involved. Other approaches have been attempted to incorporate the influence of system dynamics [18–20]. In [18], a robust H_∞ controller is developed for a piezoelectric stack actuator. In [19, 20], hysteresis compensations for piezoelectric actuators are discussed. System dynamics are modeled as lumped parameter second order differential equations. These simplifications can be adopted for applications in which the actuation direction and the excitation field direction are consistent, for example, a linear actuation stage. However, for applications like bending actuators, these models are inadequate to describe the relationship between output displacement and input field, even if the model does incorporate hysteresis effects. In this case a distributed parameter model together with the hysteretic constitutive model needs to be developed. This paper aims to develop a framework which can be used for displacement control of bending structures.

Numerical iteration needs to be used to calculate the inverse hysteretic model. This has been reported in [8, 16, 21]. Fixed stepsize of input field is selected to numerically calculate the inverse. It is demonstrated in [21] that the computational speed of the compensator depends on the iteration stepsize of input field. Higher convergence speed can be achieved by using larger stepsize. However, the control accuracy cannot be guaranteed if the stepsize is too large. Ideally, the compensator would be constructed by relating the stepsize with the inversion error so that the stepsize can be adaptively adjusted according to the varying error. In this paper, we develop a distributed parameter model which can be used for displacement control of bending structures. Also, we propose a new iteration method to calculate the compensator, in which the iteration stepsize of input field can be adaptively updated according to the inverting error. The paper is organized as follows: distributed parameter modeling is discussed in section 2. Controller design, simulation and

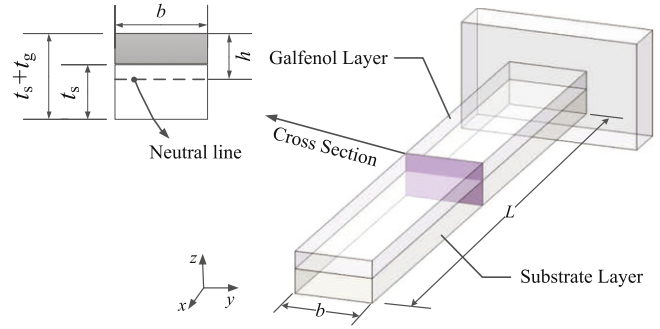


Figure 2. Geometry and coordinate system of the bending actuator.

experimental results are discussed in section 3. The conclusions are given in section 4.

2. Governing equations of the actuator

2.1. Bending actuator

The bending actuator consisting of a galfenol layer bonded to a nonmagnetic substrate is clamped at one end, while the other end is free. Figure 2 shows the geometry and the coordinates of the actuator. The x – y plane is set on the neutral plane. The structural bending theory is employed to develop the distributed parameter model. Here, we assume that the out-of-plane strain of the actuator is negligible and the Poisson's ratio of the materials is not taken into account since the length of the actuator is much greater than the width. The x -axis normal stress in the galfenol element and substrate layers can be expressed as

$$\begin{aligned}\sigma_g &= -E_g(\kappa z + \lambda), \\ \sigma_s &= -E_s \kappa z,\end{aligned}\quad (1)$$

where σ_g denotes the normal stress and κ denotes the curvature of the actuator, E is the Young's modulus, z is the distance from the neutral line, and λ is the linear magnetostriction generated by the galfenol layer. The subscript g and s represent the galfenol layer and the substrate layer, respectively. The total bending moment is calculated by integrating the differential moment due to stress over the cross-sectional area:

$$\begin{aligned}M &= - \int_{A_g} E_g(\kappa z + \lambda) z dA_g - \int_{A_s} E_s \kappa z^2 dA_s \\ &= -\kappa(E_s I_s + E_g I_g) - \left(E_g b h t_g - \frac{1}{2} E_g b t_g^2\right) \lambda \\ &= (E_s I_s + E_g I_g) \frac{\partial^2 w(x, t)}{\partial x^2} - \left(E_g b h t_g - \frac{1}{2} E_g b t_g^2\right) \lambda,\end{aligned}\quad (2)$$

where $w(x, t)$ is the vertical deflection of the neutral plane. The total shear force Q can be calculated as the differential

variation of the bending moment along the x -axis

$$\begin{aligned} Q &= \frac{\partial M}{\partial x} \\ &= (E_s I_s + E_g I_g) \frac{\partial^3 w(x, t)}{\partial x^3} \\ &\quad - \left(E_g b h t_g - \frac{1}{2} E_g b t_g^2 \right) \frac{\partial \lambda}{\partial x}. \end{aligned} \quad (3)$$

Application of force balancing gives the governing equation for the bending actuator

$$(\rho_g A_g + \rho_s A_s) \frac{\partial^2 w(x, t)}{\partial t^2} + \tilde{c} \frac{\partial w(x, t)}{\partial t} + \frac{\partial Q}{\partial x} = 0, \quad (4)$$

where \tilde{c} is the Rayleigh damping coefficient, ρ is the material density, and A is the cross area. Substitution of (3) into (4) gives

$$\begin{aligned} & (E_s I_s + E_g I_g) \frac{\partial^4 w(x, t)}{\partial x^4} + \tilde{c} \frac{\partial w(x, t)}{\partial t} \\ & + (\rho_g A_g + \rho_s A_s) \frac{\partial^2 w(x, t)}{\partial t^2} \\ & = \left(E_g b h t_g - \frac{1}{2} E_g b t_g^2 \right) \frac{\partial^2 \lambda}{\partial x^2}. \end{aligned} \quad (5)$$

Equation (5) is the distributed parameter model of the bending actuator. It is seen from (5) that the position of the neutral plane h needs to be known to determine the dynamic response. A detailed calculation of h is presented in [22]. The influence of the adhesive layer is not considered; the neutral axis can be determined by the following equation,

$$h = \frac{1}{2} \frac{\tilde{B}}{\tilde{A}} + \frac{E_s t_s t_g}{\tilde{A}} - \frac{E_g t_g \lambda_s}{\tilde{A}} \frac{1}{\kappa}, \quad (6)$$

where $\tilde{B} = E_s t_s^2 + E_g t_g^2$, $\tilde{A} = E_s t_s + E_g t_g$, and λ_s is the saturation magnetization. In order to approximate the solution of (5), the Galerkin method is employed to discretize the model. The domain of the actuator is divided into N elements, each having two nodes. The Hermite cubic interpolation functions are used to discretize equation (5),

$$\begin{aligned} \phi_1 &= 1 - 3\xi^2 + 2\xi^3, \quad \phi_2 = l_e \xi - 2l_e \xi^2 + l_e \xi^3, \\ \phi_3 &= 3\xi^2 - 2\xi^3, \quad \phi_4 = -l_e + l_e \xi^3, \end{aligned} \quad (7)$$

where l_e denotes the element length and ξ is the local spatial coordinate varying from -1 to 1 . After discretization, the globally assembled finite element equation is written as

$$[\mathbf{M}]\{\ddot{\mathbf{w}}\} + [\mathbf{C}]\{\dot{\mathbf{w}}\} + [\mathbf{K}]\{\mathbf{w}\} = \{\mathbf{F}^\lambda\} + \{\mathbf{F}^B\}, \quad (8)$$

where

$$\begin{aligned} M_{ij} &= \int_{x_e}^{x_{e+1}} (\rho_g A_g + \rho_s A_s) \phi_i \phi_j dx, \quad C_{ij} = \int_{x_e}^{x_{e+1}} \tilde{c} \phi_i \phi_j dx, \\ K_{ij} &= \int_{x_e}^{x_{e+1}} \left((E_g I_g + E_s I_s) \frac{\partial^2 \phi_i}{\partial x^2} \frac{\partial^2 \phi_j}{\partial x^2} \right) dx, \\ F_i^\lambda &= \int_{x_e}^{x_{e+1}} \left(E_g b h t_g - \frac{1}{2} E_g b t_g^2 \right) \frac{\partial^2 \lambda}{\partial x^2} \phi_i dx, \\ \{\mathbf{F}_i^B\} &= \begin{bmatrix} \left(E_g b h t_g - \frac{1}{2} E_g b t_g^2 \right) \frac{d\lambda}{dx} \Big|_{x_e} \\ - \left(E_g b h t_g - \frac{1}{2} E_g b t_g^2 \right) \lambda \Big|_{x_e} \\ - \left(E_g b h t_g - \frac{1}{2} E_g b t_g^2 \right) \frac{d\lambda}{dx} \Big|_{x_{e+1}} \\ \left(E_g b h t_g - \frac{1}{2} E_g b t_g^2 \right) \lambda \Big|_{x_{e+1}} \end{bmatrix}. \end{aligned}$$

It is seen from (8) that the load vector is a function of the magnetostriction of the galfeol layer. In order to quantify the inherent hysteresis and the material nonlinearities of the actuator, a constitutive model of galfeol is required. It can be seen from equation (8) that the structural model is linear once the magnetostriction is known. This means that more nodes in the FEM discretization will not result in more calculation burden. Most of the burden will be from the nonlinear constitutive model.

2.2. Constitutive equations

An energy averaged model for the galfeol layer is considered [23]. It is assumed that the material is composed of regions of uniform magnetization M_s called domains [24]. Domain rotation is modeled with the Stoner–Wohlfarth (SW) approximation [25]. The orientation \mathbf{m} of an SW particle can be calculated from its Gibbs free energy G which has natural dependence on the applied quantities magnetic field and stress. The internal energy of a magnetic domain with orientation $\mathbf{m} = [m_1 \ m_2 \ m_3]$ is due to the magnetocrystalline anisotropy energy, which can be expressed as [23],

$$U(\mathbf{m}) = K_4 (m_1^2 m_2^2 + m_2^2 m_3^2 + m_3^2 m_1^2), \quad (9)$$

where K_4 is the fourth-order, cubic anisotropy constant. The Gibbs free energy is [23],

$$G(\mathbf{H}, \mathbf{T}) = U(\mathbf{m}) - \boldsymbol{\lambda} \cdot \mathbf{T} - \mu_0 M_s \mathbf{m} \cdot \mathbf{H}, \quad (10)$$

where M_s is the saturation magnetization, \mathbf{T} is the six-element stress vector with the first three components the longitudinal stresses and the last three the shear stresses, \mathbf{H} is the magnetic field and $\boldsymbol{\lambda} = \boldsymbol{\lambda}(\mathbf{m})$ is the magnetostriction. It is seen that the local equilibrium domain orientations need to be determined to calculate the magnetostriction. The derivatives of the Gibbs energy with respect to \mathbf{m} give the equilibria. Further details can be found in [23]. The magnetization hysteron has six

possible field and stress dependent magnetic states. The microscopic magnetization depends on which branch of the hysteron the domain orientation resides. The hysteron is constructed by imposing an energy threshold E_t that needs to be met before the domain switches from the current branch to the branch that minimizes the energy. This threshold comes from material imperfections and anisotropy energy barriers. Material imperfections also induce an interaction field \mathbf{H}_i which is superimposed on the applied field. The magnetization of the hysteron \bar{M} in the direction \mathbf{u}_d is

$$\bar{M} = M_s \mathbf{m} \cdot \mathbf{u}_d. \quad (11)$$

The magnetostriction of the hysteron $\bar{\lambda}$ in the direction \mathbf{u}_d is

$$\begin{aligned} \bar{\lambda} = & u_{d,1}^2 \lambda_1 + u_{d,2}^2 \lambda_2 + u_{d,3}^2 \lambda_3 \\ & + u_{d,1} u_{d,2} \lambda_4 + u_{d,2} u_{d,3} \lambda_5 + u_{d,3} u_{d,1} \lambda_6. \end{aligned} \quad (12)$$

The subscripts of \mathbf{u}_d and $\boldsymbol{\lambda}$ represent the different components of the vectors. Thus the magnetization and magnetostriction of the hysteron can be written as

$$\begin{aligned} \bar{M} &= \bar{M}(\mathbf{H} + \mathbf{H}_i, \mathbf{T}, \mathbf{u}_d, E_t), \\ \bar{\lambda} &= \bar{\lambda}(\mathbf{H} + \mathbf{H}_i, \mathbf{T}, \mathbf{u}_d, E_t). \end{aligned} \quad (13)$$

To calculate the macroscopic magnetization and magnetostriction, stochastic homogenization [26] is employed with the probability density $v(E_t, \mathbf{H}_i)$, which has the combination of E_t and \mathbf{H}_i at a material point. Thus the macroscopic magnetization and magnetostriction can be calculated through stochastic homogenization of the interaction field and threshold energy [27],

$$\begin{aligned} M &= \int_{-\infty}^{\infty} \int_0^{\infty} \bar{M}(\mathbf{H} + \mathbf{H}_i, \mathbf{T}, \mathbf{u}_d, E_t) dE_t d\mathbf{H}_i, \\ \lambda &= \int_{-\infty}^{\infty} \int_0^{\infty} \bar{\lambda}(\mathbf{H} + \mathbf{H}_i, \mathbf{T}, \mathbf{u}_d, E_t) dE_t d\mathbf{H}_i. \end{aligned} \quad (14)$$

In equation (14) we assume that the energy threshold and the interaction field are exponentially and normally distributed as quantified by the densities [26],

$$v_e(E_t) = e^{-E_t/\sigma_e}, \quad (15)$$

$$v_h(\mathbf{H}_i) = e^{-\mathbf{H}_i^2/2\sigma_h^2}, \quad (16)$$

where σ_e and σ_h are positive model parameters. The physical interpretation of the stochastic distributed functions has been discussed in [26]. The density functions reflect the physical observation that the interaction field and coercive energy decay as a function of distance and guarantees that integration against the piecewise linear hysteron yields finite magnetization values. Thermal effects neglected and the temperature is assumed to be constant (room temperature) in the application. It is seen that the macroscopic magnetostriction is field and stress dependent. In order to simplify the inverse of the constitutive equation, we assume the variation of the internal stress of galferol is small and \mathbf{T} is constant when inverting (14).

It has been stated that the model is capable of describing flexible structure dynamics. To demonstrate the performance

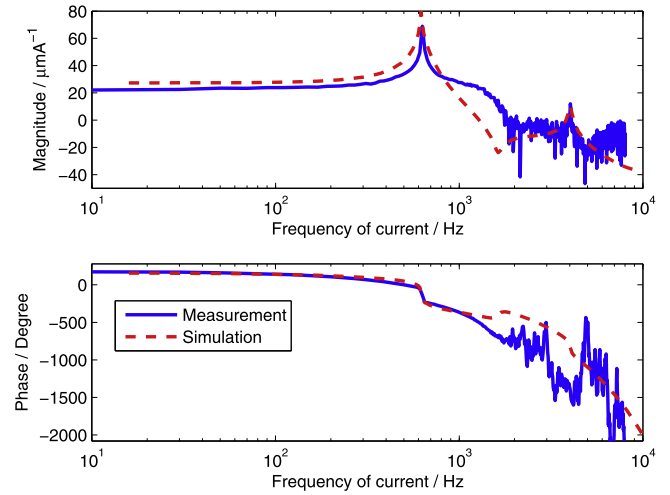


Figure 3. Measured and calculated frequency response of the bending actuator.

Table 1. Natural frequencies associated with different mode shapes.

	Predictions (Hz)	Measurements (Hz)
First mode	626	630
Second mode	4041	4030
Third mode	11640	11570

of the model, the frequency response of the bending actuator has been studied. The magnetic field is calculated with Ampere's law

$$H = \tilde{N} I_c, \quad (17)$$

where \tilde{N} is the number of turns per length of coil and I_c is the excitation current. Tip displacement of the bending actuator is calculated by the combination of equations (8), (14) and (17). Comparisons of simulation results and experimental measurements are illustrated in figure 3. It is seen that the model can effectively predict the frequency response of the bending actuator. Predictions of the first three natural frequencies are shown in table 1. The measurements consisted of a swept sine frequency response with a frequency step of 10 Hz. We have used the same discrete frequency in the simulation to calculate the frequency response. The limited sampling frequency in the simulation is the main reason that contributes to the small error in table 1.

3. Real-time control strategy

3.1. Framework of the inverse compensation

This section presents a real-time control strategy for the bending actuator using inverse compensation. The strategy is illustrated in figure 4. The desired tracking signal $y_r(t)$ is applied to the compensator which consists of the inverse of the structural model and the constitutive model. The output from the compensator is the magnetic field $u(t)$. This magnetic field will be calibrated into excitation current using the

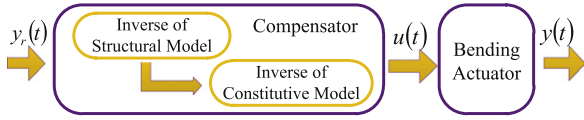


Figure 4. Scheme of the compensation.

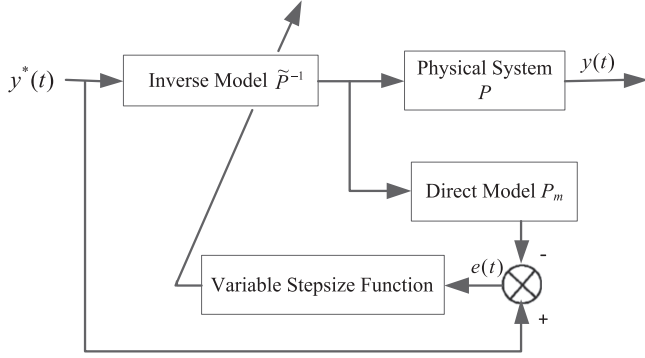


Figure 5. Scheme of the variable stepsize method.

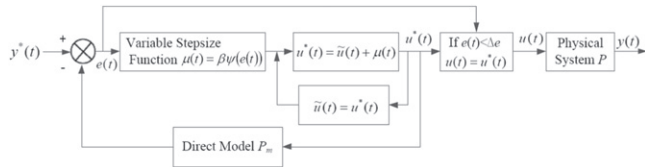


Figure 6. Flow chart of the variable stepsize method.

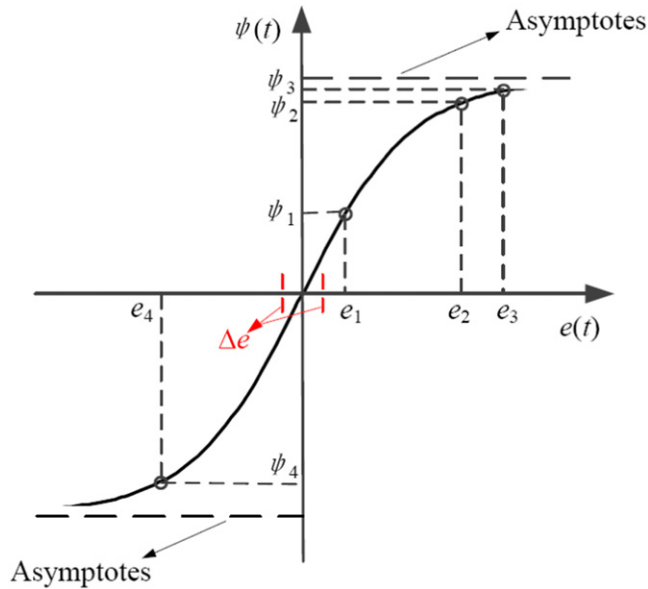


Figure 7. Value distributions of sigmoid function.

relationship $I_c = H\tilde{N}^{-1}$. The control voltage can be obtained by using an amplifier model, which will be discussed next. It should be noted that the trajectory $y_r(t)$ does not need to be known in advance. The inverse of the structural model is simple since equation (8) is a linear differential equation. When $y_r(t)$ is applied to the control system, we assume the

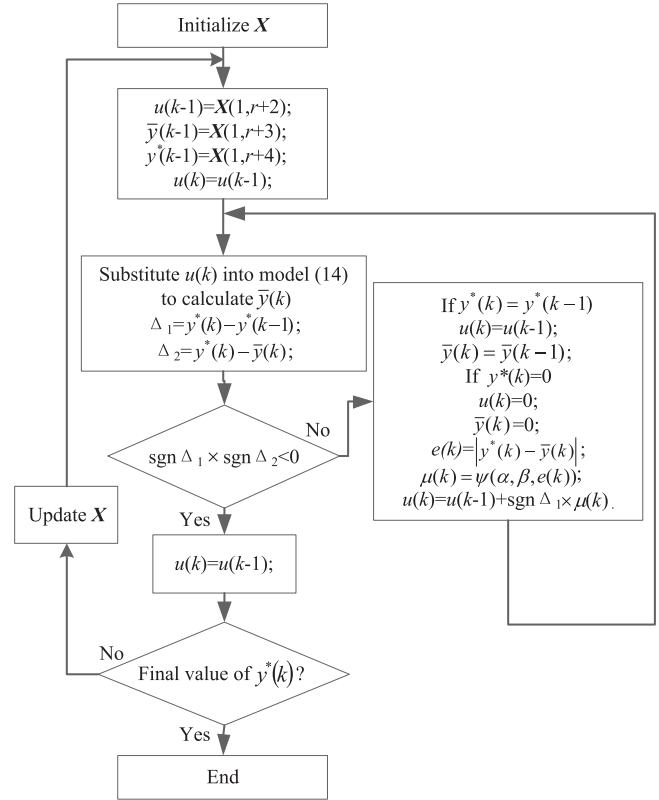


Figure 8. Flow chart for inverting the constitutive model.

magnetostriction λ calculated from the inverse of (8) is $y^*(t)$. In the following context we take $y^*(t)$ as the reference input to invert the constitutive model.

To construct the compensator, numerical iterations are needed to invert the nonlinear constitutive equation (14). It is demonstrated in [21] that the computational speed of the inverse compensator depends on the size of the step taken when advancing the forward model with larger steps increasing the speed while decreasing the accuracy. Smaller stepsize leads to higher accuracy but is computationally slower. Here we propose a variable stepsize method to develop the compensator. The stepsize can be adaptively adjusted according to the inverting error, as illustrated in figure 5.

The control signal can be written as

$$u(t) = \tilde{P}^{-1}(y^*(t), \psi(e(t))), \quad (18)$$

where P denotes the physical plant, \tilde{P}^{-1} is the inverse, and ψ is the stepsize function. It should be noted that the existence of \tilde{P}^{-1} is guaranteed by the piecewise monotonicity of hysteresis [28]. For a given magnetostriction, if the control input is either nondecreasing or nonincreasing on some time interval, the inverse of the hysteretic model can always be identified. It is seen that the control signal is a function of both the desired input and the iteration stepsize. The stepsize is a function of inverting error $e(t)$. By using (18), the output

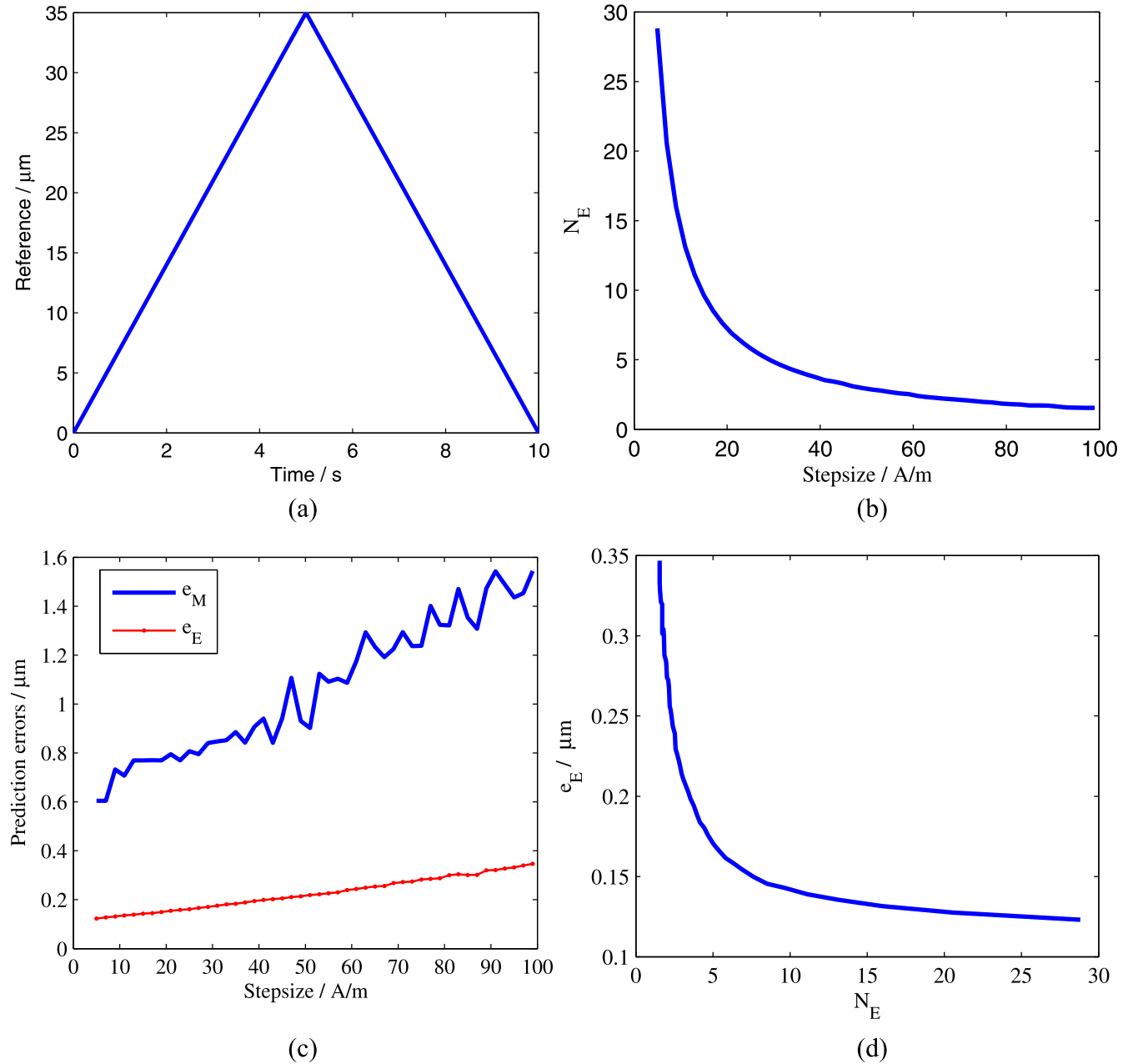


Figure 9. Simulation results for fixed stepsize method. (a) Input reference, (b) Mean value of iterations N_E using different stepsize, (c) Maximum error e_M and mean error e_E using different stepsize, (d) Mean value of error e_E versus mean value of iteration N_E .

of the actuator can be written as

$$\begin{aligned} y(t) &= P(u(t)) \\ &= P(\tilde{P}^{-1}(y^*(t), \psi(e(t)))) \end{aligned} \quad (19)$$

If the physical system P can be ideally characterized by the direct model P_m and P_m can be inverted correctly, the desired trajectory $y^*(t)$ can be completely tracked by using the scheme in figure 5.

The sigmoid function is employed to update the stepsize adaptively [29]. The function is defined as a function of the inverting error $e(t)$

$$\psi(t) = \frac{2\beta}{1 + \exp(-\alpha e(t))} - \beta, \quad (20)$$

where α and β are the two design parameters to adjust the shape and the clipping value of the saturation curve. Thus, the set of equations that define the variable stepsize method are

$$\begin{cases} e(t) = y^*(t) - P_m(u^*(t)), \\ u^*(t) = \tilde{u}(t) + \mu(t), \\ \mu(t) = \beta\psi(e(t)), \\ \psi(t) = 2\beta \cdot (1 + \exp(-\alpha |J(t)|))^{-1} - \beta, \\ J(t) = E[e^2(t)], \end{cases} \quad (21)$$

where $J(t)$ is the mean square error (MSE) of the inverting error $e(t)$ and $\mu(t)$ is the stepsize in the iteration, $u^*(t)$ is the intermediate variable defined to invert the compensator. The algorithm employed to numerically approximate equation (21)

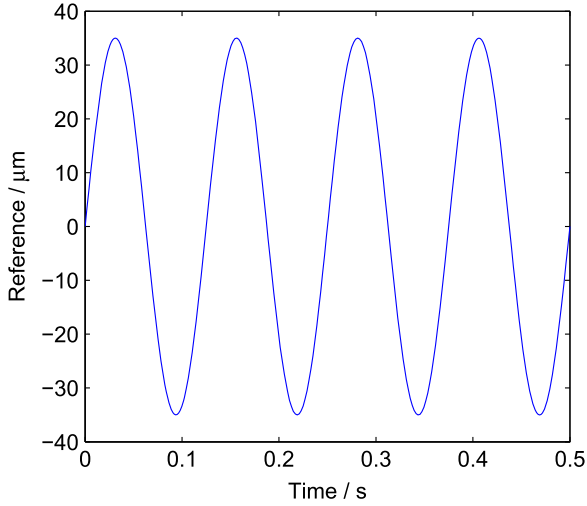


Figure 10. Reference input in the comparative simulations.

is shown in figure 6. It can be seen that the stepsize is updated via the sigmoid function $\psi(t)$, which is a function of the MSE of $e(t)$. Thus the stepsize can be adaptively updated according to the change of $e(t)$.

The value distributions of the sigmoid function are illustrated in figure 7. The function is bounded, real-valued and monotonic. The value distributions are located at the first and third quadrant, with a pair of horizontal asymptotes. The sign of the function is consistent with the sign of $e(t)$, which means that the intermediate variable $u^*(t)$ is increased if the error is positive and decreased if the error is negative. The monotonicity of the function ensures that a value of $u^*(t)$ can always be found for a given error bound Δe . Moreover, the existence of asymptotes in figure 7 guarantees that the function values will be maintained at large values if the errors are relatively large (see (e_2, ψ_2) , (e_3, ψ_3) in figure 7). If the error is decreased, $u^*(t)$ will decrease accordingly (see (e_1, ψ_1)). In this way, the stepsize has been set up to be adaptively updated according to the change of $e(t)$. Efficiency can be increased

while the inversion accuracy can be guaranteed as well. Equation (21) needs to be discretized in the time domain for the control design. The discrete form of (21) can be written as

$$\begin{cases} e(k) = y^*(k) - P_m(u^*(k+1)), \\ u^*(k+1) = \tilde{u}(k) + \mu(k), \\ \mu(k) = \beta\psi(e(k)), \\ \psi(k) = 2\beta \cdot (1 + \exp(-\alpha |J(k)|))^{-1} - \beta, \\ J(k) = e(k) \cdot e(k-1), \end{cases} \quad (22)$$

where k denotes the discrete sampling sequence number. In (22) the MSE of the inversion error $e(t)$ is replaced with the product of the two adjacent discrete data. In order to solve (22), the control signal $u(k)$ needs to be known. This can be obtained by solving the inverse of constitutive equation (14). It is discussed in section 2 that in the magnetization process the energy threshold E_t needs to be reached before the domain switches from the current orientation to the orientation that minimizes the local Gibbs energy. Also, the interaction field H_i needs to be calculated due to the material imperfections. These two parameters need to be recorded when the domains start to switch due to the applied field. For convenience, here we define a state variable $\mathbf{X}(k)$ as

$$\mathbf{X}(k) = [\mathbf{E}(E_t(k), H_i(k))_{1 \times r}, u(k), u(k-1), \bar{y}(k-1), y^*(k-1)]^T, \quad (23)$$

where $\bar{y}(k-1)$ represents the result calculated from the direct model P_m and $\mathbf{E}(E_t(k), H_i(k))_{1 \times r}$ is the column vector that records the magnetization state of the magnetic domains. The magnetization state includes two parameters, the energy threshold E_t and the interaction field H_i , which are statistically distributed parameters. The change of the two parameters is recorded with the column vector $\mathbf{E}(E_t(k), H_i(k))_{1 \times r}$. The length of the vector r depends on the number of gauss quadrature integration points used for equation (14). The total length of $\mathbf{X}(k)$ is $r+4$. The flow chart for inverting (14) is illustrated in figure 8.

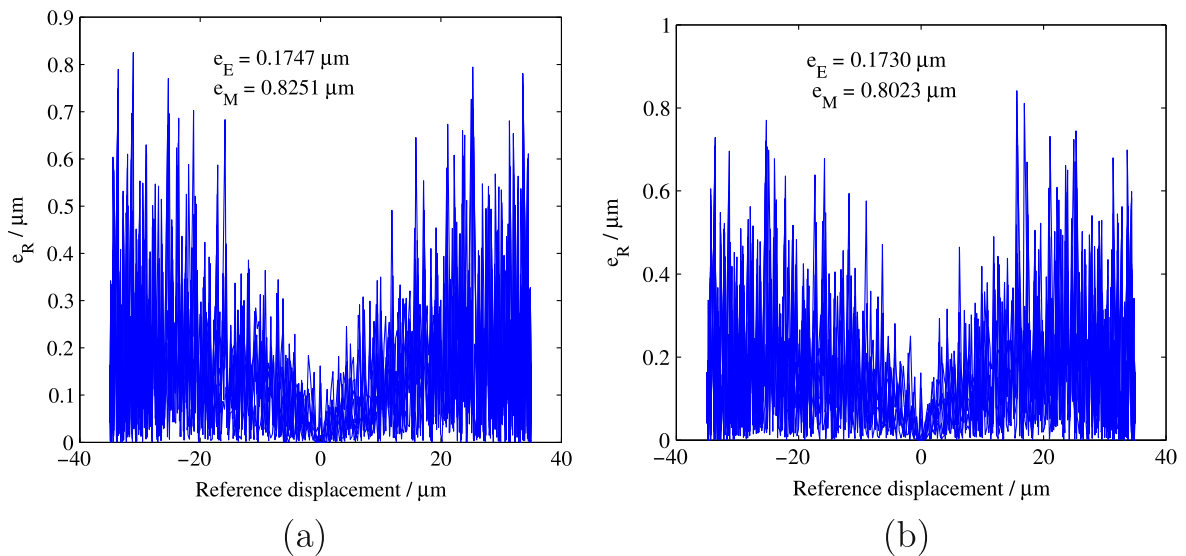


Figure 11. Prediction errors of the two methods, (a) fixed stepsize method, (b) the proposed variable stepsize method.

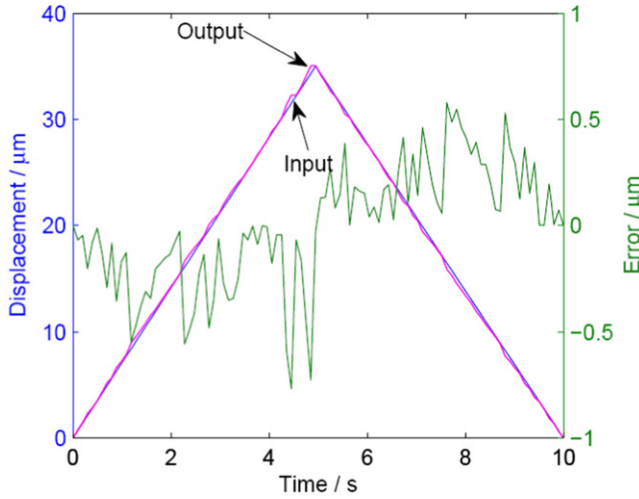


Figure 12. Output response compared with the reference input for stepsize 30 A/m.

The output from the flow chart is the magnetic field $u(t)$. Equation (17) shows the field-current relationship. The control voltage $V(t)$ can be obtained by solving the first order model of the amplifier

$$V(t) = L_c \frac{dI_c(t)}{dt} + R_c I_c(t), \quad (24)$$

where L_c is the inductance of the coil and R_c is the resistance. Thus the control voltage can be obtained when the magnetic field $u(t)$ is known from the flow chart (figure 8). In figure 8, the first step is to initialize the parameter vector \mathbf{X} . The element definition of \mathbf{X} is given by equation (23). When the desired magnetostriction $y^*(k)$ is given, the inverting error is calculated in the second step followed by a termination condition. If the termination condition is not satisfied, the value of magnetic field variable $u(k)$ will be adjusted according to the adaptively updated procedure (see equation (22)) and the updated $u(k)$ will be substituted

into (14) to generate a new magnetostriction, until the termination condition is satisfied. Then $u(k)$ will be taken as the right inverting result and accordingly the control voltage can be obtained by the following equations

$$I_c(k) = \frac{u(k)}{\tilde{N}},$$

$$V(k) = L_c \frac{I_c(k) - I_c(k-1)}{\Delta t} + R_c I_c(k), \quad (25)$$

where Δt denotes the sampling period.

3.2. Simulation results

The efficiency of the proposed strategy compared with the existing method is discussed in this section. The reference input is the tip displacement $y_d^*(t)$ and the output is the displacement $\bar{y}(t)$ calculated from the direct model P_m . It should be noted that since our model is developed in the distributed parameter form, the tip displacement is not the only option that we could choose. Any other point on the flexible structure can be selected. It has been discussed that the control accuracy is related with the iteration stepsize. In order to compare the performance of the two methods, an optimal stepsize needs to be determined to run the fixed stepsize simulation. We choose different stepsize ranging from 5 to 100 A m^{-1} and the simulation results are illustrated in figure 9. The input is a quasi-static sinusoidal signal (figure 9(a)). In order to calculate the accuracy, the maximum error, the mean error and the mean value of iterations are defined as follow

$$e_R = y_d^*(k) - \bar{y}(k), \quad (26)$$

$$e_M = \text{MAX}(y_d^*(k) - \bar{y}(k)), \quad (27)$$

$$e_E = \frac{\sum_k (y_d^*(k) - \bar{y}(k))}{N_l}, \quad (28)$$

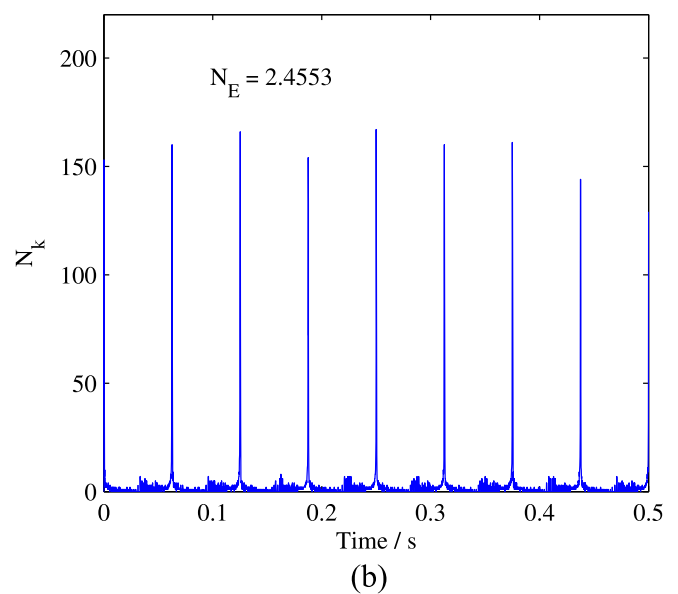
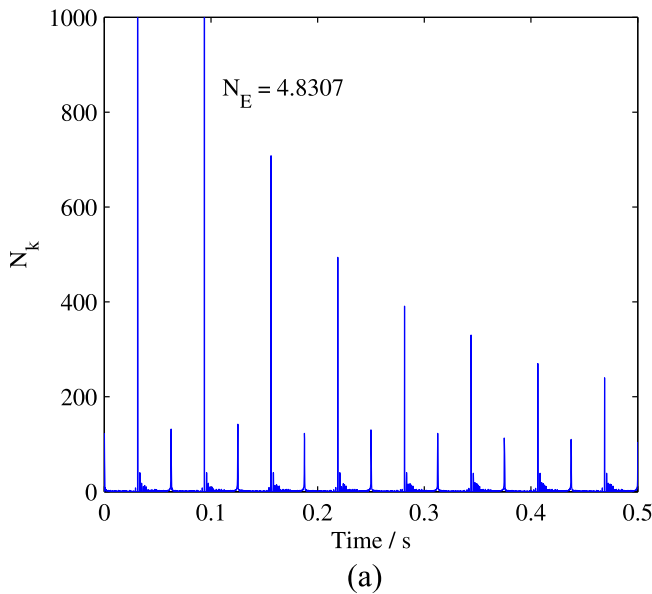


Figure 13. Iteration numbers of the two methods, (a) Fixed stepsize method, (b) The proposed variable stepsize method.

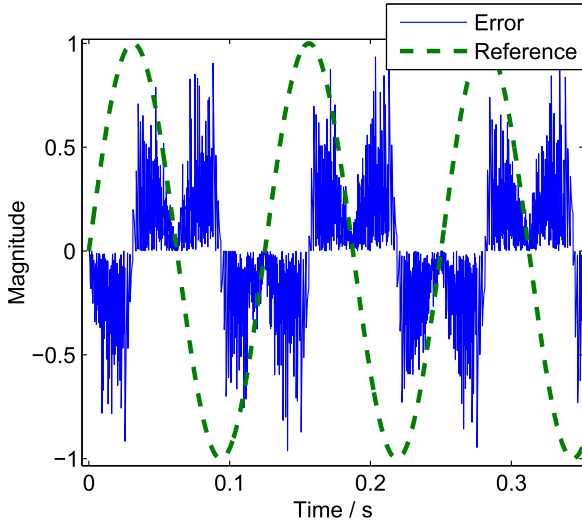


Figure 14. Calibrated reference and error in the time domain.

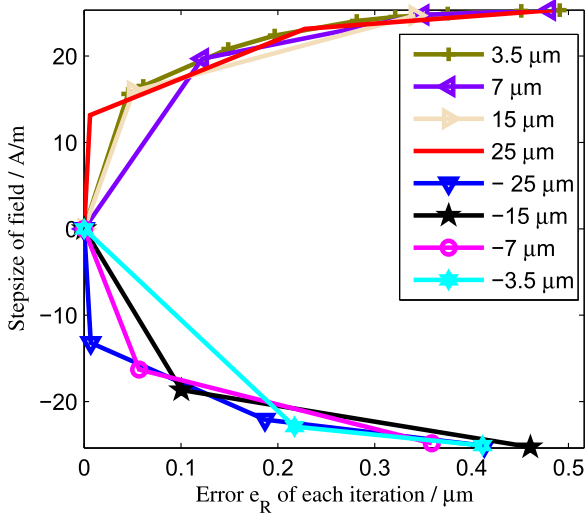


Figure 15. Convergence of stepsize according to the change of tracking error.

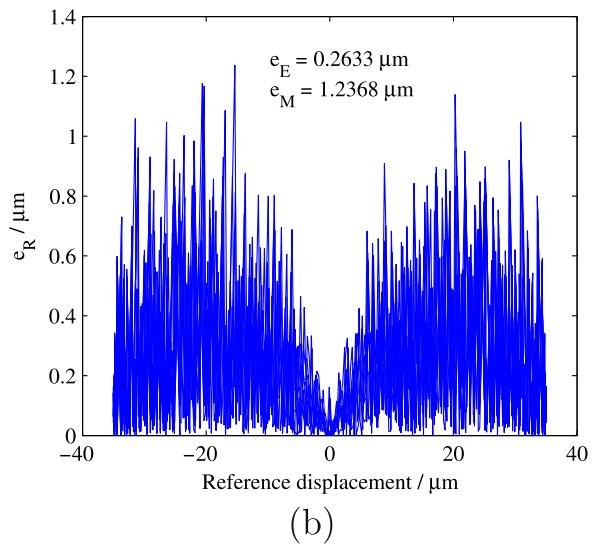
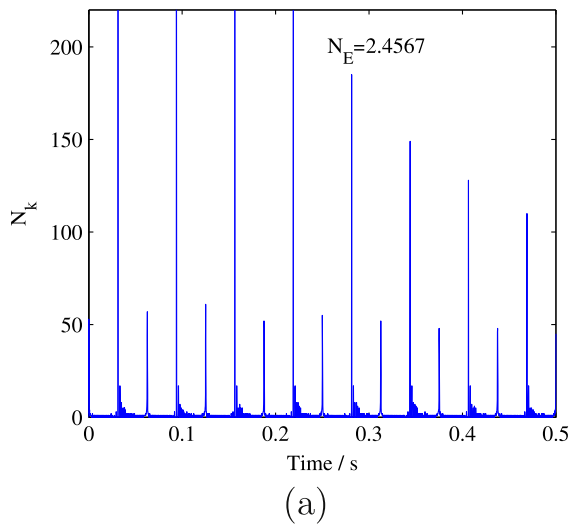


Figure 16. Simulation results by constraining the iteration numbers N_E for the fixed stepsize method, (a) N_E is constrained approximately the same with the iterations in figures 13(b) and (b) the prediction error e_R calculated with constrained iterations.

$$N_E = \frac{\sum_{k=1}^{N_l} N_k}{N_l}, \quad (29)$$

where e_M is the maximum error, e_E is the mean error, N_E is the mean value of iterations, N_k denotes the iteration numbers used in figure 8 to satisfy the termination condition for one $y^*(k)$, and N_l is the total number of sampling points. It can be seen from figure 9(b) that the iteration number decreases with increasing the stepsize. The slope of the decrease is large when the stepsize is small. After the stepsize reaches 50 A m^{-1} , the change of the iteration numbers tends to be stable and the steady state value is around 3.2. From figure 9(c) it is seen that the change of the error is approximately linear respect to the stepsize. Figure 9(d) shows that small error e_E can be obtained by increasing the iteration numbers. To achieve the balance between the efficiency and the accuracy, we choose 30 A m^{-1} as the optimal value in the fixed stepsize iteration. Here we use 30 A m^{-1} to run the tracking control simulation for the reference input in figure 9(a). The output response is compared with the reference input and the result is shown in figure 12. It is seen that the reference input can be tracked with small errors and these errors are consistent with the values illustrated in figure 9(c). A comparison is made between the proposed variable stepsize method and a fixed stepsize. The reference input is chosen as the ac excitation signal illustrated in figure 10. The simulation results are shown in figures 11 and 13. In order to compare the magnitude of the errors, we have taken the errors in figure 11 as the absolute values. Calibrated reference and errors in the time domain are plotted in figure 14.

Figure 11 shows the prediction errors of the two methods. It is seen from the figure that the error e_R increases with increasing the magnitude of the reference. This is because of the termination condition we used in the flow chart (figure 8). If the reference magnitude is monotonically increasing, the control voltage will increase continuously until the current

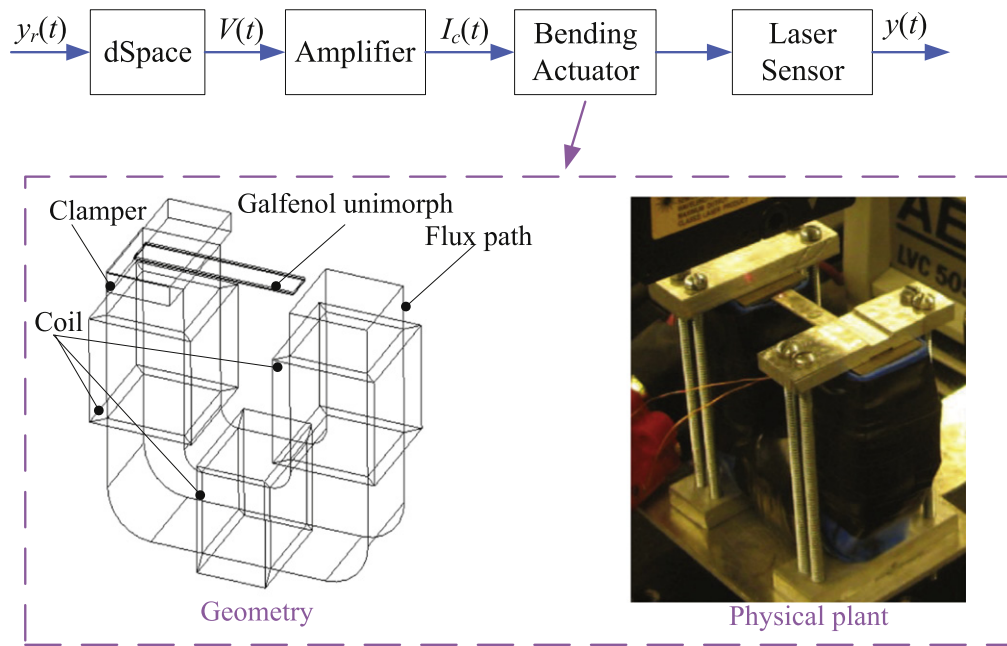


Figure 17. Experimental procedure and diagram of the bending actuator.

Table 2. Dimension and elastic properties of the bending actuator.

Parameter	Galfenol	Substrate (Brass)
Thickness	0.381 mm	0.3 mm
Length	25 mm	25 mm
Young's modulus	$6 \times 10^{10} \text{ N m}^{-1}$	$1.1 \times 10^{11} \text{ N m}^{-1}$

output is larger than the input. Usually this will result in relatively larger errors for larger reference magnitude. However, this termination condition gives much faster convergence speed than setting up a single tolerance. From figure 11 the errors calculated with the variable stepsize method are slightly smaller than the fixed stepsize method, but the differences are very small. This means that if we use an optimized value for the fixed stepsize method (30 A m^{-1} in our case), both of the methods can achieve good accuracy. However, the iteration efficiency will be different.

Figure 13 compares the iteration efficiencies of the two methods where the iteration number N_k is plotted as a function of time. This is because for each discrete sampling reference $y^*(k)$, numerical iteration N_k is needed to determine the corresponding $u(k)$ (see figure 8). Thus, N_k can be plotted as a function of time when the inverting process is completed. The maximum value of N_k in figure 13(a) exceeds 1000 and the maximum value of N_k in figure 13(b) is less than 180. The mean values N_E for the two plots are 4.8307 and 2.4553, which means the iteration efficiency has been increased by 49.17% by using our method. Comparing figures 11 and 13 we can find out that both of the methods can achieve good control accuracy. However, the proposed variable stepsize method supplies much higher efficiency than the existing fixed stepsize method.

Convergence of the stepsize has been plotted in figure 15. We have selected several reference points (see legends in

figure 15) from the continuous signal to demonstrate the convergence process. It is seen from the figure that the stepsize can be adaptively updated according to the change error e_R . If e_R is relatively large, the stepsize is maintained at a large value. This is helpful to accelerate the convergence speed. When the error goes smaller, the change of the stepsize becomes faster and iteration can be terminated rapidly. These changings are guaranteed by the properties of sigmoid function we discussed in section 3.1.

In figures 11 and 13 we have constrained the stepsize to be the optimal value in the fixed stepsize simulation to investigate the efficiency. Next we are going to investigate the prediction error for the two methods when the iteration efficiency is constrained. In order to constrain the efficiency, we increase the stepsize value starting from 30 A m^{-1} until the iteration number N_E for the fixed stepsize simulation is approximately the same with the proposed variable stepsize method. The simulation results are illustrated in figure 16. The mean value of iterations N_E in figure 16(a) is 2.4567, which is approximately the same with the value in figure 13(b). It can be seen from figure 16(a) that maximum value of N_k exceeds 220. The mean error e_E and the maximum error e_M in figure 16(b) are 34.3% and 35.1% larger than the values in figure 11(b), which means that if the same efficiency is required for the computation, the proposed method can achieve higher inversion accuracy.

3.3. Experimental results

The experimental setup comprises a dSpace ControlDesk system, a displacement laser sensor, a linear current amplifier and a galfenol bending actuator. The experimental procedure is illustrated in figure 17. A control voltage is generated from the dSpace system and the excitation current is applied to the

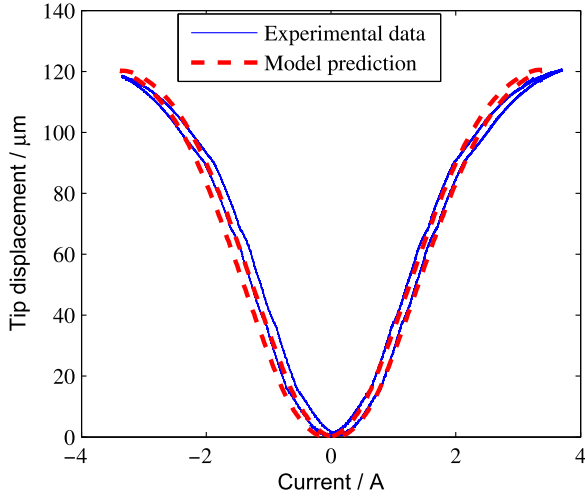


Figure 18. Quasi-static validation of the bending actuator.

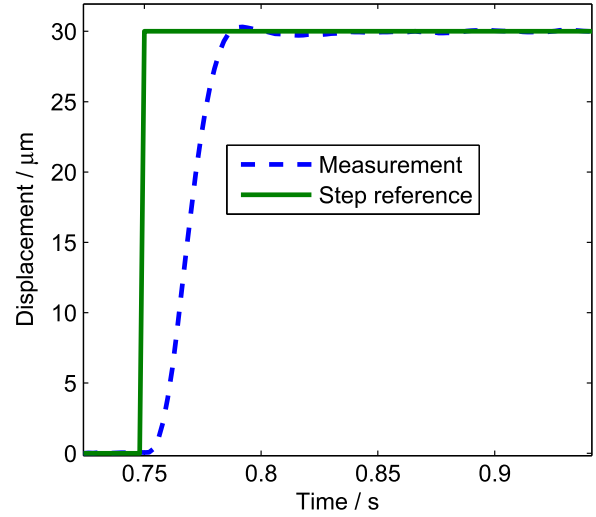


Figure 19. Step response of the PID controller.

Table 3. Parameters used in the constitutive model.

Symbol	Parameters	Values
σ_e	Parameter of the energy threshold distribution	0.4 kJ m^{-3}
σ_h	Parameter of the interaction field distribution	3000 A m^{-1}
T_0	Magnitude of the bias stress	21.3 MPa
K_4	Anisotropy constant	20 kJ m^{-3}
M_s	Saturation magnetization	$1.1698 \times 10^6 \text{ A m}^{-1}$
λ_{100}	Magnetostriction in $\langle 100 \rangle$ direction	$2/3 \times 260 \text{ ppm}$
λ_{111}	Magnetostriction in $\langle 111 \rangle$ direction	$2/3 \times (-20) \text{ ppm}$

bending actuator via the amplifier. The output displacement is measured with a laser sensor.

The magnetic path of the bending actuator is composed of laminated electric steel and the thicknesses of galfeol and substrate are very thin (0.381 mm). Eddy currents are thus considered to be negligible. The dimensions and the elastic properties of the bending actuator are illustrated in table 2. In order to set up the controller, model parameters need to be identified with quasi-static measurement. A 0.1 Hz sinusoidal signal is used to excite the actuator and the measurement result is illustrated in figure 18. The model prediction is calculated by using equations (8) and (14) and the linear field-current relationship (17). It can be seen from figure 18 that a full hysteresis loop is attained in the quasi-static measurement. The hysteresis and the saturation can be described by the direct model. Since there is no bias magnetic field, the tip displacement of the actuator demonstrates the butterfly-type nonlinearity. The model parameters identified from figure 18 are illustrated in table 3. These parameters are used to set up the real-time controller.

In order to run the comparative experiments, a well-tuned PID controller has been developed to compare the performance with the proposed controller. The step response test is performed first to identify the controller parameters.

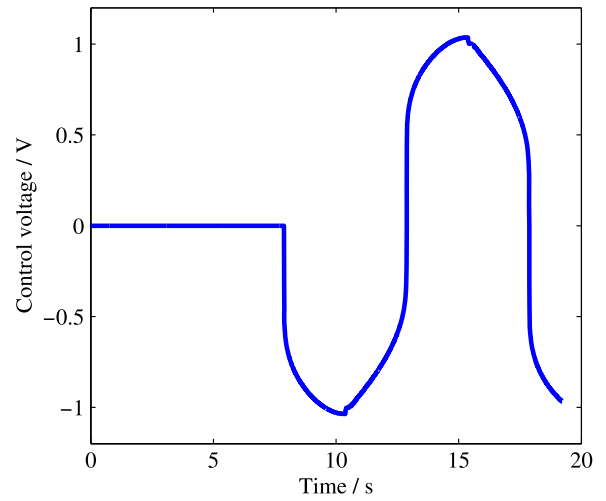


Figure 20. Control voltage of the quasi-static tracking.

Experimental results are shown in figure 19 and the parameters are identified as follows, $K_p = 0.05$, $K_i = 2.5$ and $K_d = 0.0002$. It is seen in figure 19 that the steady state error is almost zero and there is no obvious overshoot. The settling time is about 0.05 s. Control experiments of the proposed controller are conducted at 0.1 and 10 Hz. The tracking results are illustrated in figures 18–20. It should be noted that the control framework we have developed in this paper is based on the distributed parameter model, which offers the advantage that displacement at any point of the bending structure can be studied, not just the tip displacement. In figure 22, we have used the proposed controller to control both the tip displacement and the displacement midway from the tip, without changing parameters. It can be seen from figure 20 that the reference trajectory can be precisely tracked by using the inverse strategy. The nonlinearity is observed from the control voltage in figures 20 and 21(c). This shows that the nonlinearity of the bending actuator can be described by the inverse compensator and the control voltage demonstrates the

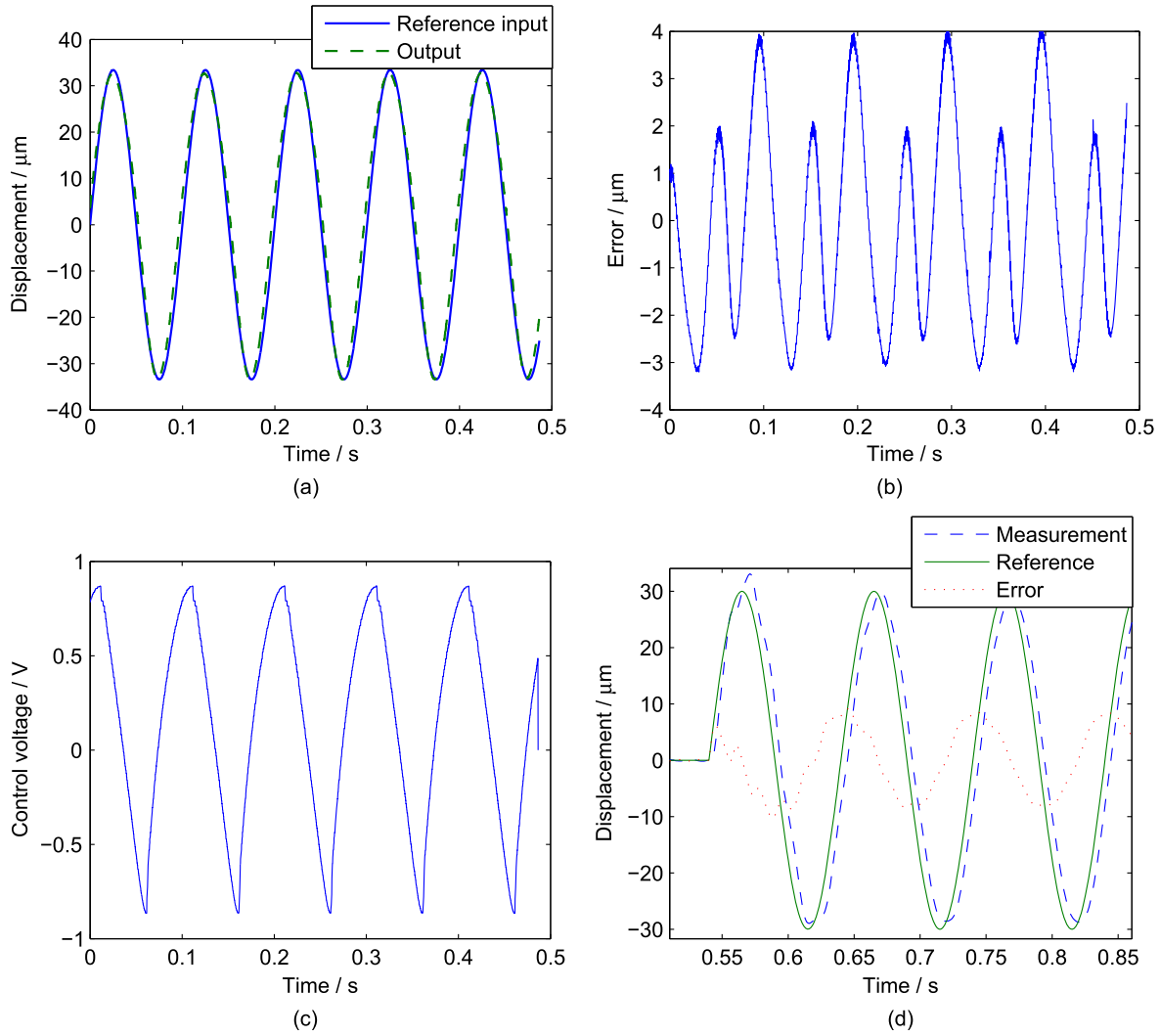


Figure 21. Tracking results of 10 Hz sinusoidal reference for different controllers, (a) control result for the proposed controller, (b) control error of the proposed controller, (c) control voltage of the proposed controller, (d) control result for the PID controller.

nonlinearity that can be used to compensate the nonlinearity of galfenol. Thus the linear relationship of reference input and output can be obtained.

The error in figure 21(b) is larger than the quasi-static result. This is because the control parameters are identified from the quasi-static measurements. Model parameters could vary in the dynamic case due to system dynamics. We assume in equation (14) that the variation of the internal stress of galfenol is small and the stress is constant when inverting (14). In the dynamic case the influence of the internal stress is one of the reasons contributed to the error in figure 21(b). Tracking results of the PID controller at 10 Hz are illustrated in figure 21(d). It is seen that there is a phase lag between the reference and the output displacement. This is the main reason contributed to the errors of the PID controller.

Experimental results of tracking a more complicated trajectory for the proposed controller is illustrated in figure 23. The trajectory is generated with a random source generator. It is seen that the trajectory can be tracked with good accuracy. Errors around sharp corners are relatively larger than the smooth regions. This is because of the

termination condition used in the controller. At sharp corners, the change of the reference is no longer monotonous, which means the sign of the stepsize might be changed in the iteration process and the error will be larger than the monotonous region. This is consistent with the errors observed in the simulation results (figure 14). The errors around the reference peaks are relatively larger than those located in the monotonous regions.

4. Conclusions

This paper addresses the dynamic modeling of a galfenol bending actuator and the real-time control strategy. System dynamics is modeled with a distributed parameter equation instead of a lumped parameter model. In order to increase the computation efficiency, a variable stepsize method has been proposed to adaptively update the stepsize in the iteration. Simulation results show that the iteration efficiency has been increased by 49.17% by using the method. If the efficiencies of the two methods are constrained approximately the

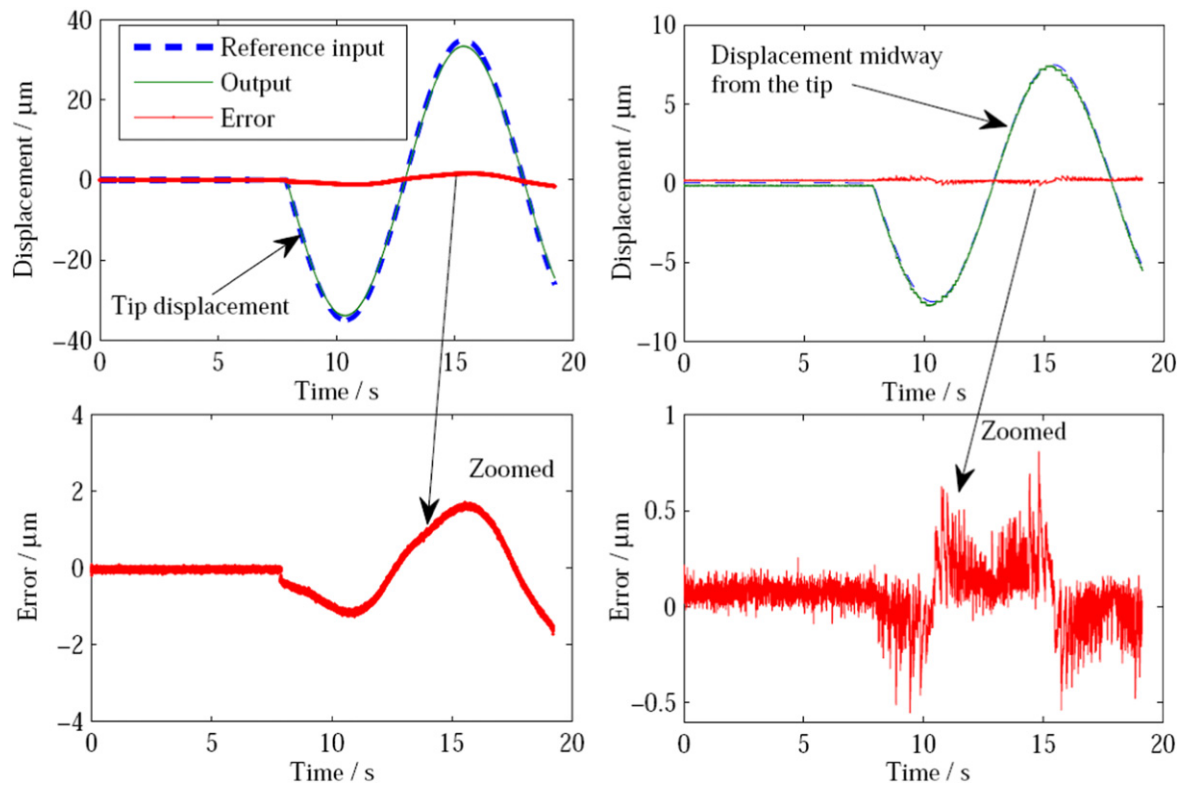


Figure 22. Tracking results of the quasi-static trajectory of the proposed controller.

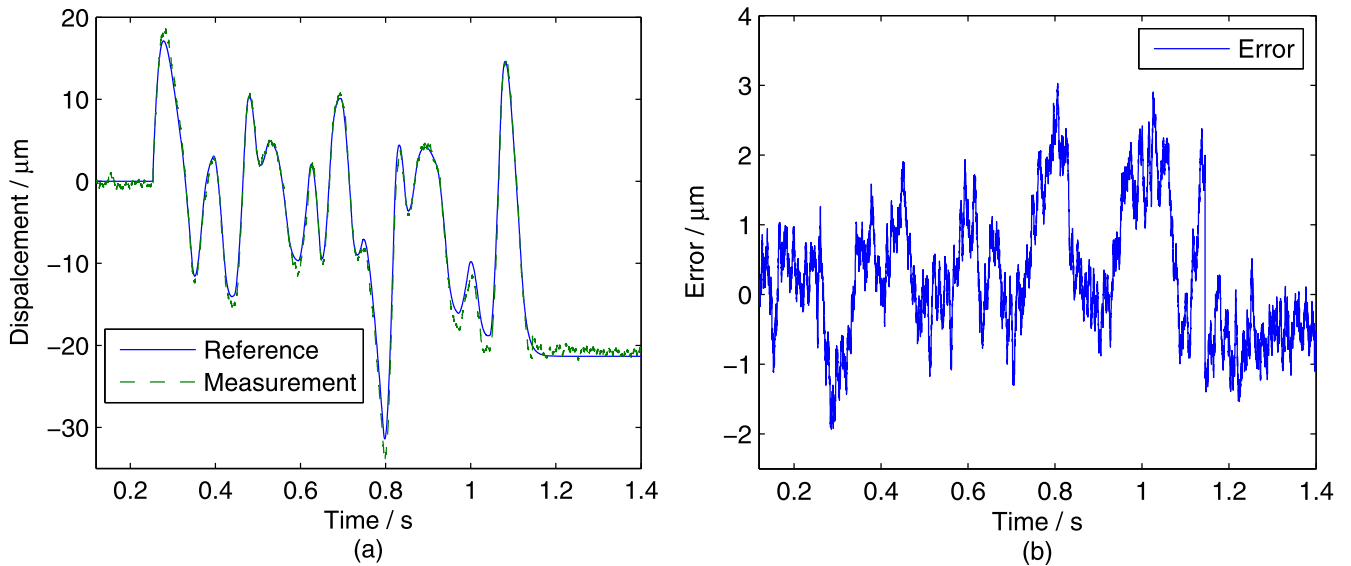


Figure 23. Tracking results of the trajectory generated with a random source generator, (a) reference input and physical measurement, (b) control error.

same, it is shown that the tracking error of the fixed stepsize method is higher than the variable stepsize over 30%. The real-time control experiments are conducted at different frequencies. It is shown that the reference input can be tracked by using the strategy. Tracking error is larger at higher frequency. The assumption that the variation of the internal stress of galphenol is small is one of the reasons contributed to the error.

Acknowledgments

The authors acknowledge the financial support provided by the National Natural Science Foundation of China (51205293, 51175395), the Natural Science Foundation of Zhejiang Province (LY15E050011) and China Postdoctoral Science Foundation (2015M571904).

References

- [1] Karafi M R, Hojjat Y and Sassani F 2013 A new hybrid longitudinal-torsional magnetostrictive ultrasonic transducer *Smart Mater. Struct.* **22** 065013
- [2] Case D, Taheri B and Richer E 2014 Dynamical modeling and experimental study of a small-scale magnetorheological damper *IEEE/ASME Trans. Mech.* **19** 1015–24
- [3] Li L Y, Zhang C M, Yan B P, Zhang L and Li X P 2011 Research of fast-response giant magnetostrictive actuator for space propulsion system *IEEE Trans. Plasma Sci.* **39** 744–8
- [4] Chopra I 2000 Status of application of smart structures technology to rotorcraft systems *J. Helicopter Soc.* **45** 228–52
- [5] Hardee H C and Hardee N L 1997 Magnetostrictive-driven fretting machines for interconnection research *J. Alloys Compd.* **258** 83–6
- [6] Evans P G and Dapino M J 2008 State-space constitutive model for magnetization and magnetostriction of galferol alloys *IEEE Trans. Magn.* **44** 1711–20
- [7] Atulasimha J and Flatau A B 2011 A review of magnetostrictive iron–gallium alloys *Smart Mater. Struct.* **20** 043001
- [8] Hatch A G, Smith R C, De T and Salapaka M V 2006 Construction and experimental implementation of a model-based inverse filter to attenuate hysteresis in ferroelectric transducers *IEEE Trans. Control Syst. Technol.* **14** 1058–69
- [9] Chen X K, Su C Y and Fukuda T 2008 Adaptive control for the systems preceded by hysteresis *IEEE Trans. Autom. Control* **53** 1019–25
- [10] Panusittikorn W and Ro P I 2008 Modeling and control of a magnetostrictive tool servo system *J. Dyn. Syst. -T. ASME.* **130** 031003
- [11] Oates W S, Evans P G, Smith R C and Dapino M 2009 Experimental implementation of a hybrid nonlinear control design for magnetostrictive actuators *Trans. ASME, J. Dyn. Syst. Meas. Control* **131** 041004
- [12] Zhang X L and Tan Y H 2008 Modeling hysteresis and its inverse model using neural networks based on expanded input space method *IEEE Trans. Control Syst. Technol.* **16** 484–90
- [13] Aljanaideh O, Janaideh M A, Rakheja S and Su C Y 2013 Compensation of rate-dependent hysteresis nonlinearities in a magnetostrictive actuator using an inverse Prandtl–Ishlinskii model *Smart Mater. Struct.* **22** 025027
- [14] Zhang J, Merced E, Sepulveda N and Tan X B 2014 Modeling and inverse compensation of nonmonotonic hysteresis in VO₂-coated microactuators *IEEE/ASME Trans. Mechatronics* **19** 579–88
- [15] Choi S B, Seong M S and Ha S H 2013 Accurate position control of a flexible arm using a piezoactuator associated with a hysteresis compensator *Smart Mater. Struct.* **22** 045009
- [16] Iyer R V, Tan X B and Krishnaprasad P S 2005 Approximate inversion of the Preisach hysteresis operator with application to control of smart actuators *IEEE Trans. Autom. Control* **50** 798–810
- [17] Tan X B and Baras J S 2005 Adaptive identification and control of hysteresis in smart materials *IEEE Trans. Autom. Control* **50** 827–39
- [18] Chuang N and Petersen I R 2013 Robust H control of hysteresis in a piezoelectric stack actuator *J. Dyn. Syst.-T. ASME* **135** 064501
- [19] Chen X D and Li W 2015 A monolithic self-sensing precision stage: design, modeling, calibration, and hysteresis compensation *IEEE/ASME Trans. Mechatronics* **20** 812–23
- [20] Juhsz L, Maas J and Borovac B 2011 Parameter identification and hysteresis compensation of embedded piezoelectric stack actuators *Mechatronics* **21** 329–38
- [21] Nealis J M and Smith R C 2007 Model-based robust control design for magnetostrictive transducers operating in hysteretic and nonlinear regimes *IEEE Trans. Control Syst. Technol.* **15** 22–39
- [22] Shu L, Dapino M J, Evans P G, Chen D F and Lu Q G 2011 Optimization and dynamic modeling of galferol unimorphs *J. Intell. Mater. Syst. Struct.* **22** 781–93
- [23] Evans P G and Dapino M J 2009 Efficient model for field-induced magnetization and magnetostriction of galferol *J. Appl. Phys.* **105** 113901
- [24] Jiles D C 2010 *Introduction to Magnetism and Magnetic Materials* 2nd edn (London: Taylor and Francis)
- [25] Liorzou F, Phelps B and Atherton D L 2000 Macroscopic models of magnetization *IEEE Trans. Magn.* **36** 418–28
- [26] Smith R C, Dapino M J, Braun T and Mortensen A 2006 A homogenized energy framework for ferromagnetic hysteresis *IEEE Trans. Magn.* **42** 1747–69
- [27] Evans P G and Dapino M J 2013 Measurement and modeling of magnetic hysteresis under field and stress application in iron–gallium alloys *J. Magn. Magn. Mater.* **330** 37–48
- [28] Tan X B and Baras J 2004 Modeling and control of hysteresis in magnetostrictive actuators *Automatica* **40** 1469–80
- [29] Fu J and Zhu W P 2008 A nonlinear acoustic echo canceller using sigmoid transform in conjunction with RLS algorithm *IEEE Trans. Circuits II* **55** 1056–60